Research Square

Preprints are preliminary reports that have not undergone peer review.
They should not be considered conclusive, used to inform clinical practice,
or referenced by the media as validated information.

Multi-objective optimization method for hybrid isolation systems using explicit seismic response prediction

Tianci Li

925158964@qq.com

Yunnan Land and Resources Vocational College https://orcid.org/0009-0007-2387-990X

Ruiming Liu

Kashi university

Qian Li

Yunnan Land and Resources Vocational College

Guangyu Sun

Kunming University of Science and Technology

Research Article

Keywords: hybrid isolation system, viscous damper, energy balance, explicit seismic response prediction, multi-objective optimization

Posted Date: June 17th, 2026

DOI: https://doi.org/10.21203/rs.3.rs-9725832/v1

License: This work is licensed under a Creative Commons Attribution 4.0 International License.
Read Full License

Multi-objective optimization method for hybrid isolation systems using explicit seismic response prediction

Tianci Li[1], Ruiming Liu[2,3,*], Qian Li[1] and Guangyu Sun[4]

1 Yunnan Land and Resources Vocational College, Kunming 650500, China; gtzyxyrszp@163.com

2 School of Civil Engineering, Kashi University, Kashi 844008, China

3 Xinjiang Key Laboratory of Engineering Materials and Structural Safety, Kashi University, Kashi 844000, China

4 Faculty of Civil Engineering and Mechanics, Kunming University of Science and Technology, Kunming 650500, China

** Correspondence: 18787012526@163.com*

Multi-objective optimization method for hybrid isolation systems using explicit seismic response prediction

Abstract: In highly seismic regions, a hybrid isolation system integrating isolators and viscous dampers can achieve both isolation efficiency and displacement control. However, the quantitative design of damper parameters lacks theoretical guidance. To address this bottleneck, this study proposes a multi-objective optimization design method balancing isolation-layer displacement and total shear control. First, based on the energy balance equation, explicit mappings of the displacement response ratio and shear response ratio versus the added damping ratio are derived. These mappings allow direct estimation of structural responses. Then, a design framework based on minimizing a weighted sum function is established, from which the optimal added damping ratio can be determined according to engineering needs. Case validation demonstrates that the explicit formulas yield predictions within a 20% deviation compared with time-history analysis results, meeting the accuracy requirements of preliminary design. The weighting method effectively balances displacement and shear control, significantly reducing the design iteration cost caused by repeated trial computations in time-history analysis. This method offers a practical tool for the preliminary design of low-to-medium-rise isolated structures and lays a methodological foundation for the analytical optimization design of complex isolation systems.

Keywords: hybrid isolation system; viscous damper; energy balance; explicit seismic response prediction; multi-objective optimization

1 Introduction

Conventional seismic design relies on increasing member sections to enhance structural stiffness and resist seismic forces. However, in highly seismic regions, this "hard-resistance" strategy often leads to overly large column sections and amplified seismic demands, making it difficult to meet the performance requirements of key protected structures [1-3]. In contrast, base isolation—introducing a flexible layer beneath the structure to elongate the fundamental period away from the dominant frequency range of ground motions—fundamentally reduces the seismic response of the superstructure [4-7]. However, application in highly seismic regions introduces an inherent trade-off between isolation efficiency and displacement control. Using smaller-diameter isolators lowers isolation-layer stiffness and improves efficiency but risks excessive displacement and bearing rupture; larger-diameter isolators constrain displacement but increase stiffness, thereby diminishing isolation efficiency. This dilemma has become a major bottleneck for applying isolation technology in high-seismicity zones [8-10]. To address this challenge, a hybrid isolation system combining lead rubber bearings (LRBs) and viscous fluid dampers (VFDs) in parallel has been proposed (Fig. 1). In this system, VFDs dissipate substantial seismic energy and effectively limit isolation-layer displacement without appreciably increasing stiffness, thereby achieving synergistic optimization of isolation efficiency and displacement control. Such hybrid systems

have recently become a research focus in structural vibration control [11-14]. However, there is still a lack of systematic theoretical guidance for the quantitative design of VFD parameters to optimally balance this trade-off.

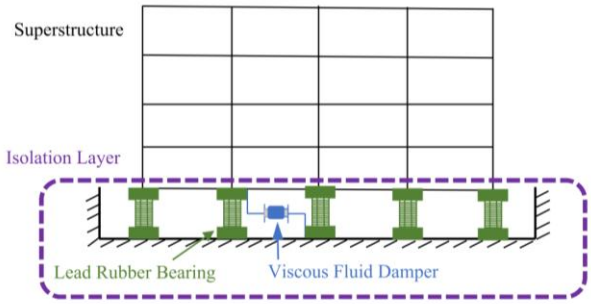


Figure 1. Parallel hybrid isolation system with LRBs and VFDs.

Extensive research efforts have been devoted to the theoretical modeling, performance validation, and optimal design of hybrid systems. At the modeling level, Naeim and Kelly [15,16] laid the foundation for calculating the equivalent stiffness and damping ratios of LRBs. Makris et al. [17,18] systematically reviewed the early development of isolation technology and emphasized the theoretical advantages of velocity-dependent dampers in isolation layers. Kitayama and Constantinou [19,20] further examined how inherent damping modeling affects the prediction accuracy of isolated structures, emphasizing the applicability boundary of equivalent linearization under large displacement amplitudes. De Domenico et al. [21,22] proposed an improved equivalent linearization model for VFD-isolator combinations based on random vibration theory, and validated its accuracy via nonlinear time-history analyses. However, most of the aforementioned models rely on the assumption that dampers alone dissipate all seismic energy [23]. This assumption often leads to overly conservative designs and precludes explicit formulation of the mapping between damper parameters and structural response.

For performance validation, numerous numerical and experimental studies have confirmed the superiority of combining LRBs with VFDs. Ozer and Inel [24] conducted 528 bidirectional nonlinear time-history analyses. They demonstrated that the LRB-VFD combination reduced displacement and acceleration demands by over 74% in a torsionally irregular RC building and nearly eliminated its torsional response. Liu, Wang, et al. [25,26] systematically validated the excellent seismic performance of hybrid isolation systems via full-scale shaking table tests. Habieb et al. [27,28] conducted finite element analyses on masonry structures and likewise confirmed the clear advantages of this hybrid scheme in protecting structural members and enhancing seismic capacity. Li et al. [29,30] further noted that a single isolation measure often fails to meet the performance control requirements of complex structures, whereas an improved hybrid isolation configuration can effectively address this limitation. Despite these multifaceted validations, the determination of damper parameters is still largely dependent on an iterative trial-and-correction procedure. Specifically, a set of damper properties is assumed first; then, time-history analyses are conducted to evaluate structural response. The parameters are subsequently adjusted and rechecked until predefined performance limits are met. This approach involves considerable computational cost and provides limited physical insight, which impedes the rapid preliminary estimation of damper characteristics needed to achieve specified performance objectives.

In the field of design optimization methods, research focus has gradually shifted from single-criterion control to multi-objective collaborative optimization. Alwilly and Lavan [31] proposed a gradient-based

optimization framework to simultaneously optimize the isolator layer position, stiffness, and damper parameters. This framework minimizes cost while satisfying displacement and acceleration constraints. Charmpis et al. [32,33] employed a genetic algorithm to optimize the vertical arrangement of the isolation layer, aiming to minimize absolute acceleration while ensuring that inter-story drift and isolation-layer displacement meet prescribed limits. Skandalos et al. [34,35] developed a multi-objective optimization method to simultaneously minimize the inter-story drift of the superstructure and the displacement of the isolation layer. The aforementioned methods either minimize a single response index or rely on iterative searches based on intelligent algorithms. However, minimizing a single indicator fails to adequately capture the coupling relationship between isolation-layer displacement and base shear. Consequently, the resulting designs often deviate from a well-balanced engineering trade-off. Although intelligent algorithms can handle multiple objectives, they lack an analytical link between damping parameters and structural response. This requires computationally expensive iterative searches whenever design conditions change. A truly explicit multi-objective optimization framework remains absent [32,34,36-38].

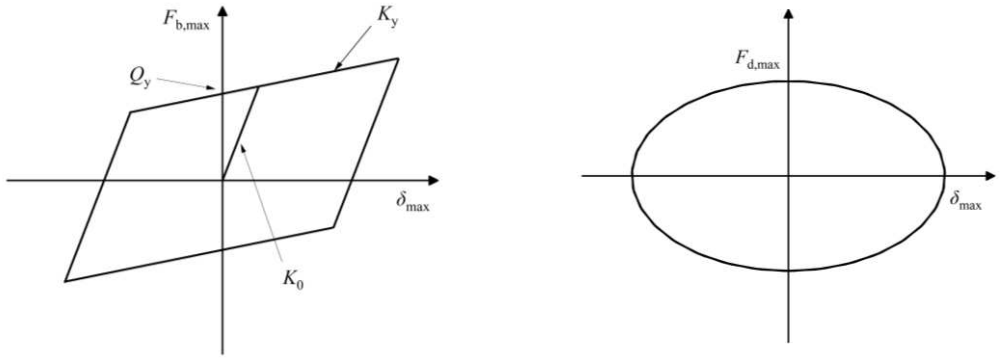
In summary, although existing studies have achieved significant progress in various subfields of hybrid isolation systems, the aforementioned limitations are highly interrelated. At the theoretical level, no explicit mapping exists between damper parameters and structural response. This shortcoming forces performance validation to depend on trial computations rather than rapid estimation approaches. Consequently, the optimization design level struggles to establish a multi-objective explicit framework. This logical disconnection across the three levels implies that the optimization design theory for dampers still lacks a systematic solution grounded in an energy-coordination mechanism—an urgent and promising research direction [39-41].

To address the limitations in existing research, this paper focuses on a hybrid isolation system composed of LRBs and VFDs connected in parallel. Its objective is to develop an analytically explicit and multi-objective collaborative design optimization method. First, based on the energy balance equation at the end of an earthquake, explicit mappings are derived from the added damping ratio to both the displacement response ratio and the total shear response ratio of the isolation layer. This will yield simple prediction formulas that directly estimate the structural response under Maximum Considered Earthquake (MCE) from damper parameters. Second, to overcome the common limitation of single-criterion methods, a minimization design approach based on a linear weighted sum function is proposed. By adjusting the weighting coefficients according to project requirements, designers can directly determine the optimal added damping ratio and corresponding seismic response estimates, realizing a shift from "single-criterion control" to "multi-objective collaborative optimization." Finally, a seven-story frame structure in Kashi, Xinjiang, will be used as a case study for the optimization design and time-history verification of the hybrid isolation system. Overall validation will be conducted based on comparisons with and without dampers, response analyses for various weighting combinations, and theoretical prediction accuracy. It is expected that the proposed method can significantly reduce design iteration cost without sacrificing prediction accuracy, providing a theoretical basis and practical tool for the preliminary design of low-to-medium regularly isolated structures. More importantly, the theoretical framework established herein, which links energy balance, response mapping, and multi-objective optimization, provides an extensible methodological basis for the analytical optimization design of complex isolation systems.

2 Response prediction for hybrid isolation systems based on energy method

2.1 Derivation of energy balance equations and key responses

This study focuses on the shear-type model [42]. The force-deformation characteristics of the isolation layer components, including additional viscous dampers, are shown in Fig. 2. Subscripts *b* and *d* denote the lead rubber bearing and the viscous damper, respectively. The pre-yield and post-yield stiffnesses of the lead rubber bearing are denoted by K_0 and Ky, respectively. The shear force of the bearing is denoted as F_b, and its maximum value is $F_{b,max.}$ The viscous damper exhibits linear velocity-dependent behavior, with a damping coefficient of *C. Its* output force under seismic excitation is F_d, and the peak output is $F_{d,\,max.}$ The total shear force of the isolation layer is denoted as F, and its maximum value is $F_{max.}$ The displacement of the isolation layer is denoted as δ, and its maximum value as $\delta_{max.}$ The fundamental period and frequency of the superstructure are T_f and ω_f, respectively. The total mass of the superstructure is M. To simplify the derivation while ensuring a conservative design, we assume that the input seismic energy is entirely dissipated by the isolation layer.



(a) Hysteretic curve of the lead-core laminated rubber bearing (LRB)

(b) Hysteresis curve of the viscous fluid damper (VFD)

Figure 2. Force-displacement relationship of the isolation component.

Due to the phase difference between the peak forces of the viscous damper and the isolation bearing, the maximum total shear force of the isolation layer is not the simple algebraic sum of these two components. Under harmonic excitation, the shear force-displacement relationship of a damper can be characterized by an elliptical equation

$$\frac{\delta^2}{\delta_{max}^2}+\frac{F_d^2}{F_{d,max}^2}=1 \qquad (1)$$

Accordingly, the total shear force F in the isolation layer at any time instant can be expressed as

$$F=F_b+F_d=K_{eq}\delta\pm\frac{F_{d,max}}{\delta_{max}}\sqrt{\delta_{max}^2-\delta^2} \qquad (2)$$

where K_{eq} denotes the equivalent lateral stiffness of the isolation system.

By taking the extremum of Equation (2), the maximum shear force of the isolation layer F_{max} can be related to the maximum shear forces of the bearing $F_{b,max}$ and the damper $F_{d,max}$ as

$$F_{\max} = \sqrt{F_{\mathrm{b,max}}^2 + F_{\mathrm{d,max}}^2} \quad (3)$$

Three shear coefficients are defined: α_{b} for the isolation bearing, α_{d} for the viscous damper, and α_1 for the total isolation layer, as given in Eq. (4).

$$\alpha_{\mathrm{b}} = \frac{F_{\mathrm{b,max}}}{M\mathrm{g}} \quad \alpha_{\mathrm{d}} = \frac{F_{\mathrm{d,max}}}{M\mathrm{g}} \quad \alpha_1 = \frac{F_{\max}}{M\mathrm{g}} \quad (4)$$

Equation (3) shows that the coefficients satisfy the following relationship

$$\alpha_1 = \sqrt{\alpha_{\mathrm{b}}^2 + \alpha_{\mathrm{d}}^2} \quad (5)$$

By the time the structure ceases to vibrate after seismic excitation, all elastic strain energy has been fully dissipated. The energy balance equation for the base-isolated structure with a viscous damper in the isolation layer at rest is

$$W_{\mathrm{d,h}}(t) + W_{\mathrm{b,h}}(t) = E(t) \quad (6)$$

In this equation, $W_{\mathrm{d,h}}$ and $W_{\mathrm{b,h}}$ denote the energy dissipation of the viscous damper and isolation bearing, respectively, while E denotes the seismic input energy.

Reference response quantities are introduced to define the reference displacement δ_0 and shear coefficient α_0 for the isolation story with only isolation bearings. For a pure isolation system, the energy equation yields

$$\pi n_{\mathrm{b}} \varsigma_{\mathrm{eq,300}} K_{\mathrm{eq,300}} \delta_0^2 = \frac{M V_{\mathrm{E}}^2}{2} = E(t) \quad (7)$$

Simplifying gives

$$\delta_0 = V_{\mathrm{E}} T_{\mathrm{f,300}} \sqrt{\frac{1}{8\pi^3 n_{\mathrm{b}} \varsigma_{\mathrm{eq,300}}}} \quad (8) \qquad \alpha_0 = \frac{V_{\mathrm{E}}}{T_{\mathrm{f,300}} g} \sqrt{\frac{2\pi}{n_{\mathrm{b}} \varsigma_{\mathrm{eq,300}}}} \quad (9)$$

In this equation, n_{b} denotes the number of hysteretic cycles undergone by the seismic isolation bearings; $K_{\mathrm{eq,300}}$ denotes the equivalent stiffness of the isolation layer without dampers. It is determined under a reference state where the isolation system deformation equals three times the bearing thickness, based on which the corresponding fundamental period $T_{\mathrm{f,300}}$ and equivalent damping ratio $\zeta_{\mathrm{eq,300}}$ are derived. The velocity equivalent of seismic input energy is represented by V_{E}. Based on these definitions, the displacement response ratio $R_{\mathrm{D}}=\delta\max/\delta_0$ is introduced to characterize the peak displacement of the isolation layer with viscous dampers relative to that without dampers. Similarly, the total shear force response ratio is defined as $R_{\mathrm{V}} = \alpha_1 / \alpha_0$. The total energy dissipation of the viscous dampers can be expressed as

$$W_{\mathrm{d,h}}(t_0) = n_{\mathrm{d}} \pi \mathrm{F}_{\mathrm{d,max}} \delta_{\max} \quad (10)$$

where n_{d} denotes the equivalent number of hysteretic cycles at the displacement amplitude corresponding to the energy dissipated by the viscous dampers.

The parameter η_d denotes the energy dissipation ratio of viscous dampers, which is defined as $\eta_d = W_{d,h}/(W_{d,h}+W_{b,h})$. This ratio characterizes the fraction of energy dissipated by the dampers with respect to the total system energy. On the basis of this definition, the energy balance yields Equation (11)

$$n_d \pi \alpha_d M g \delta_{max} = \frac{M V_E^2}{2} \eta_d \quad (11)$$

Substituting Eqs. (7) and (10) into Eq. (11) yields

$$\frac{\alpha_d}{\alpha_0}\frac{\alpha_b}{\alpha_0}\frac{n_d}{n_b}\frac{1}{\varsigma_{eq,300}}\left(\frac{T_{100}}{T_{300}}\right)^2 = \eta_d \quad (12)$$

Therefore, the ratio of the shear coefficient α_b of bearings to the reference shear coefficient α_0 (i.e., α_b/α_0) can be expressed in terms of α_d as follows

$$\frac{\alpha_b}{\alpha_0}\left(\frac{T_{100}}{T_{300}}\right)^2 = \frac{\alpha_0}{\alpha_d}\frac{n_b}{n_d}\varsigma_{eq,300}\eta_d \quad (13)$$

In addition, the maximum displacement δ_{max} and α_b satisfy the following relationship

$$\frac{\delta_{max}}{\delta_0} = \frac{\alpha_b Mg / K_{eq,100}}{\alpha_0 Mg / K_{eq,300}} = \frac{\alpha_b}{\alpha_0}\frac{K_{eq,300}}{K_{eq,100}} = \frac{\alpha_b}{\alpha_0}\left(\frac{T_{100}}{T_{300}}\right)^2 \quad (14)$$

In a hybrid isolation system equipped with dampers, the deformation of the isolation layer is reduced due to the displacement restriction provided by the dampers. Accordingly, $K_{eq,100}$ and $T_{f,100}$ are defined based on the reference state where the deformation reaches the bearing thickness, representing the equivalent stiffness and the corresponding fundamental period of the structure, respectively.

The displacement response ratio R_D is expressed as

$$R_D = \frac{\delta_{max}}{\delta_0} = \frac{\alpha_b}{\alpha_0}\left(\frac{T_{100}}{T_{300}}\right)^2 = \frac{\alpha_0}{\alpha_d}\frac{n_b}{n_d}\varsigma_{eq,300}\eta_d \quad (15)$$

Based on Eq. (5), the total shear response ratio R_V can be written as

$$R_V = \frac{\alpha_1}{\alpha_0} = \sqrt{\left(\frac{n_b}{n_d}\varsigma_{eq,300}\eta_d\frac{T_{300}^2}{T_{100}^2}\right)^2\left(\frac{\alpha_0}{\alpha_d}\right)^2 + \left(\frac{\alpha_d}{\alpha_0}\right)^2} \quad (16)$$

Accordingly, once α_d is determined, Eq. (15) yields the predicted maximum displacement of the isolation layer, while Eq. (16) provides the predicted maximum total shear.

Assuming harmonic motion $y = \delta_{max}\sin(\omega_{eq}t)$ with amplitude δ_{max} and equivalent frequency ω_{eq}, the maximum output force $F_{d,max}$ of a viscous damper under earthquake excitation can be expressed in terms of the added damping ratio ζ_d introduced by the damper to the system as

$$F_{d,max} = c w_{eq}\delta_{max} = 2\zeta_d m w_{f,100} w_{eq}\frac{F_{b,max}}{m w_{f,100}^2} = 2\zeta_d\frac{w_{eq}}{w_{f,100}}F_{b,max} \quad (17)$$

Combining Eqs. (4), (13), and (17), the expression for α_d in terms of the added damping ratio ζ_d is obtained as

$$\frac{\alpha_d}{\alpha_0} = \frac{T_{300}}{T_{100}}\sqrt{2\zeta_d\frac{w_{eq}}{w_{f,100}}\frac{n_b}{n_d}\varsigma_{eq,300}\eta_d} \quad (18)$$

2.2 Key parameter calibration using time-history analysis

2.2.1 Case study model and ground motion inputs

A six-storey frame model is constructed having uniform floor height of 3.3 m and uniform mass distribution along the story heights. The isolation layer is located on top of the foundation consisting of lead–rubber bearings with equivalent lateral stiffnesses of 1.985 kN/mm and 2.7 kN/mm corresponding to the fundamental periods of 2.5 s and 2.9 s, respectively. The added damping ratio provided by viscous dampers is taken as the primary variable, ranging from 0.05 to 1.0 in increments of 0.05, 0.1, 0.2, 0.3, 0.4, 0.5, 0.6, 0.7, 0.8, 0.9, and 1.0. Ground motions representative of high-intensity seismic regions are considered, with a peak acceleration of 510 cm/s² and a site characteristic period of 0.45 s, based on which seven artificial accelerograms are generated. As shown in Fig. 3, these seven artificial waves slightly exceed the code-specified response spectrum [43] in long period range, which keeps the input seismic energy stable.

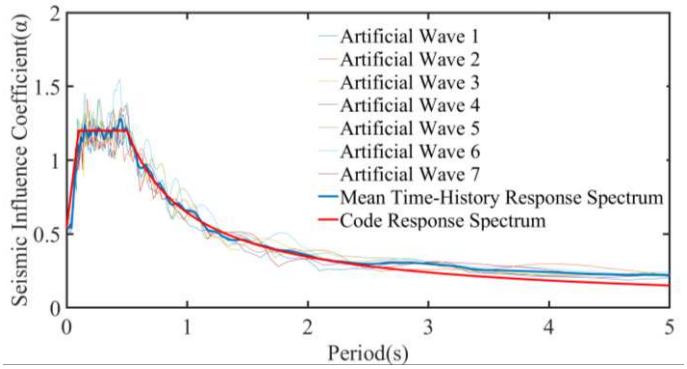


Figure 3. Comparison of seven time history response spectra and code response spectrum. (α_{max}=1.2, T_g=0.45s)

2.2.2 Calibration of the number of hysteretic cycles

In the seismic energy analysis of isolated structures, the number of hysteretic cycles is a parameter that links the input seismic energy to the energy dissipation capacity by dampers. For the hybrid isolation system consisting of LRBs and VFDs in parallel, two parameters should be identified, i.e., the equivalent number of hysteretic cycles n_b for LRBs in the isolation-bearing-only system and the equivalent number of cycles n_d for VFDs in the hybrid system. Since the two parameters have different definitions, they should be calibrated separately according to the specific design procedure.

For the isolation-bearing-only system, the value of n_b is determined by the selected ground motions records. After the type of bearing is selected according to the design code, the time history analyses are conducted using multiple site-compatible ground motion records. For each record, the ratio of total hysteretic energy dissipated by the LRB to the per-cycle dissipated energy is computed. Results indicate that the mean value of the ratio over the selected ground motions is 3.9 and the dispersion is low, so it can be used as the input parameter for subsequent theoretical analyses. From the energy dissipation mechanism perspective, plastic heat generated in the LRB lead core under cyclic deformation induces strength degradation, thereby limiting the number of effective energy dissipation cycles. Kalpakidis and Constantinou [44,45] demonstrated that the effective cycle number of the lead core is controlled by the thermal equilibrium mechanism under typical ground motion duration. Their statistically stable value is in good agreement with the 3.9 value obtained in this study, verifying the physical rationality of the proposed parameter.

For the hybrid isolation system, the value of n_d is obtained through time history analyses of the structure equipped with dampers under the same set of ground motions. For each motion, the ratio of the total energy dissipated by dampers to the energy dissipated per cycle at the corresponding displacement amplitude is calculated. The results indicate that the mean value of n_d for the hybrid system is 1.5. This finding is comparable with values reported in the literature. For isolation systems consisting of elastomeric bearings and viscous dampers, a prior study [46] recommended that the equivalent number of cycles for viscous dampers is taken as 2.0 when the structural fundamental period is $\leqslant$ 5 s. The slightly lower value of 1.5 obtained herein is primarily attributed to the LRBs sharing part of the seismic input energy, thereby reducing both the energy demand and the equivalent number of cycles for the VFDs.

This difference shows the collaborative energy dissipation mechanism in parallel by LRBs and VFDs.

Based on time history analyses with selected ground motions, the values n_b=3.9 and n_d=1.5 are determined in this study, both of which agree well with findings reported in authoritative studies, providing reliable input parameters for subsequent response prediction based on energy balance.

2.2.3 Fitting of energy dissipation ratio η_d to added damping ratio ζ_d

In energy-balance analyses of hybrid isolation systems, the energy dissipation ratio η_d of viscous dampers is a key parameter correlating the added damping ratio ζ_d with the system's energy distribution. η_d characterizes the contribution of viscous dampers to the global energy dissipation mechanism and is strongly correlated with parameters including the damping coefficient and damping exponent [47,48]. A quantitative relationship between η_d and ζ_d is established via time-history analyses using seven ground motions compatible with the site conditions. Numerical results of η_d for various ζ_d values are presented in Fig. 4.

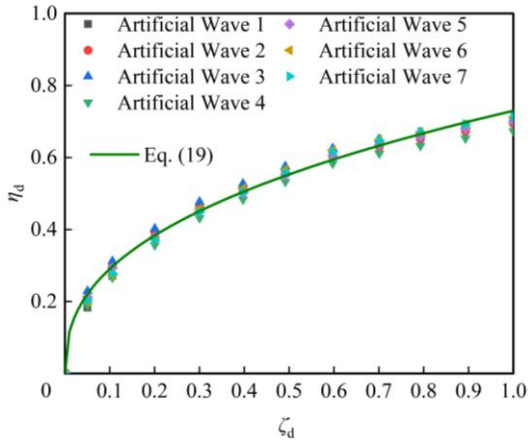


Figure 4. Variation of energy dissipation ratio with damping ratio.

A power function is used to fit the data points, yielding

$$\eta_d = 0.73\zeta_d^{0.4} \quad (19)$$

The coefficient of determination R^2=0.98 indicates a good fit.

The fitted function is physically reasonable: η_d=0 when ζ_d=0, satisfying the boundary condition ζ_d=0 $\rightarrow\eta_d$=0. The exponent 0.4 is between 0 and 1. It represents the sublinear behavior: the growth rate of dissipation ratio decreases when ζ_d increases. From a constitutive perspective, the force-velocity relationship of viscous dampers inherently follows a power-law model $F=CV^{\alpha}$, which is well validated by

extensive experimental studies [49,50]. At the energy level, a power-function description of the relationship between damper dissipation and damping ratio is widely adopted, owing to the inherent nonlinearity of the energy balance equation. This approach is commonly used in modeling damping-related parameters [51-53]. The fitting results obtained herein agree well with fundamental energy dissipation theory and provide a theoretical basis for subsequent design optimization.

2.3 Derivation and assessment of response prediction formulae for the isolation layer

This yields the expression for predicting α_d from ζ_d

$$\frac{\alpha_d}{\alpha_0} = A\zeta_d^{0.7} \quad (20)$$

with the coefficient A given by

$$A = \frac{T_{300}}{T_{100}}\sqrt{2X0.73\frac{w_{eq}}{w_{f,100}}\frac{n_b}{n_d}\varsigma_{eq,300}}$$

Following the derivation in Eq. (18), the ratio of the structural fundamental frequency to the equivalent excitation frequency, ω_f/ω_{eq}, is expressed as

$$\frac{w_f}{w_{eq}} = \left(\frac{T_{300}}{T_{100}}\right)^2 2\zeta_d\frac{n_b}{n_d}\zeta_{eq,300}\eta_d\left(\frac{\alpha_0}{\alpha_d}\right)^2 \quad (21)$$

Substituting the time-history analysis results into the right-hand side of Eq. (19) yields the distribution of ω_f/ω_{eq} under different ground motions, as shown in Fig. 5. The results indicate that, unlike in isolated systems using rubber bearings, the equivalent excitation frequency in a hybrid isolation system combining lead-rubber bearings and viscous fluid dampers is significantly less influenced by the added damping ratio $\zeta_d$provided by the VFDs. Previous experimental studies have shown that the shear behavior of LRBs is insensitive to loading frequency, which is the least influential factor affecting their mechanical properties [54–57]. Accordingly, for low damping ratios (ζ_d < 1.0), the frequency ratio ω_f/ω_{eq} remains within a relatively narrow band, with a mean value of approximately 0.9 for all cases analyzed. This suggests that variations in the added damping ratio of VFDs exert little influence on the equivalent excitation frequency of the hybrid isolation system.

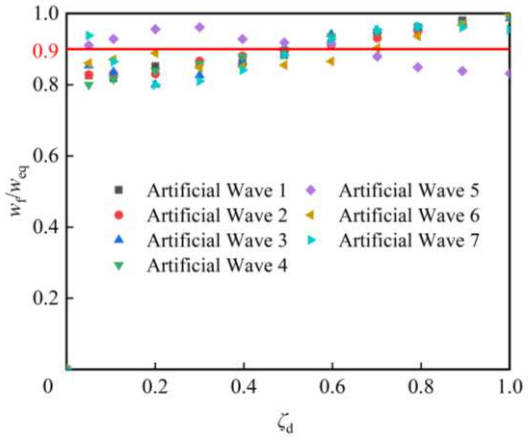


Figure 5. Frequency ratio versus damping ratio.

A comparison between the damping distribution from time-history analysis and that predicted by Eq. (20) is shown in Fig. 6. It is evident that Eq. (20) effectively captures the relationship between damping demand and added damping ratio under various ground motions for ζ_d<1.0, and can therefore be adopted to estimate the damper force output in the isolation layer.

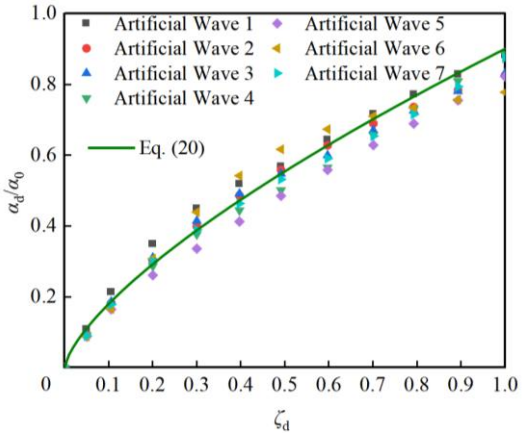


Figure 6. Variation of the damping amount with damping ratio.

Substituting Eq. (20) into Eq. (15) yields a predictive expression for the displacement response ratio R_D, and thereby for the maximum isolation layer displacement δ_{max}, as a function of the added damping ratio ζ_d

$$R_D = \frac{\delta_{max}}{\delta_0} = B\zeta_d^{-0.3} \qquad (22)$$

Here, the coefficient B is defined as

$$B = \frac{T_{100}}{T_{300}}\sqrt{\frac{0.73\zeta_{eq,300}}{2}\frac{n_b}{n_d}\frac{w_f}{w_{eq}}}$$

Substituting Eq. (20) into Eq. (16) yields the predictive expression for the total shear response ratio R_v, and thereby for the total shear force of the isolation layer, as a function of the added damping ratio ζ_d

$$R_v = \frac{\alpha_1}{\alpha_0} = \sqrt{C\zeta_d^{-0.6} + D\zeta_d^{1.4}} \qquad (23)$$

The coefficients C and D are defined as

$$C = \frac{0.73}{2}\frac{n_b}{n_d}\zeta_{eq,300}\left(\frac{T_{300}}{T_{100}}\right)^2\frac{w_f}{w_{eq}}, \quad D = 2X0.73\frac{w_{eq}}{w_f}\frac{n_b}{n_d}\zeta_{eq,300}\left(\frac{T_{300}}{T_{100}}\right)^2.$$

Table 1 compares the damper force, isolation layer displacement and total shear force derived from time-history analyses with the corresponding values predicted by Eqs. (20), (22) and (23) at added damping ratios of 0.2, 0.4 and 0.6. Evaluations based on seven ground motion records (AW1–AW7) reveal favorable agreement between theoretical predictions and time-history results at varying added damping ratios. As the added damping ratio increases, both the damper force and total shear force of the isolation layer increase, while the isolation layer displacement presents a large decrease. This trend aligns with the fundamental principles of seismic isolation and energy dissipation design. The deviations of theoretical value and time-history result are generally within an acceptable range for all cases. For the low damping ratio case (0.2), the isolation layer shear error is slightly larger; however, the error gradually converges as the damping ratio

rises to 0.4 and 0.6. The prediction error of displacement and total shear force is within ±10% for most of the ground motions, which shows a favorable prediction accuracy.

Table 1. Comparison of structural responses under MCE for different damping ratios.

Time history record	Key responses under MCE	ζd=0.2 Time-history average	ζd=0.2 Predicted value	ζd=0.2 Difference (%)	ζd=0.4 Time-history average	ζd=0.4 Predicted value	ζd=0.4 Difference (%)	ζd=0.6 Time-history average	ζd=0.6 Predicted value	ζd=0.6 Difference (%)
AW1	F_d (kN)	4830	4030	-17%	7165	6547	-9%	8889	8695	-2%
	δ_{max} (mm)	222	211	-5%	159	172	8%	142	152	7%
	F_1 (kN)	11043	10968	-1%	10807	10911	1%	13434	12050	-10%
AW2	F_d (kN)	4166	4030	-3%	6714	6547	-2%	8673	8695	0%
	δ_{max} (mm)	217	211	-3%	188	172	-9%	159	152	-4%
	F_1 (kN)	10647	10968	3%	11332	10911	-4%	12619	12050	-5%
AW3	F_d (kN)	4288	4030	-6%	6783	6547	-3%	8279	8695	5%
	δ_{max} (mm)	212	211	0%	192	172	-10%	174	152	-12%
	F_1 (kN)	10632	10968	3%	11975	10911	-9%	13254	12050	-9%
AW4	F_d (kN)	3962	4030	2%	6136	6547	7%	7808	8695	11%
	δ_{max} (mm)	225	211	-6%	184	172	-7%	163	152	-7%
	F_1 (kN)	11309	10968	-3%	11742	10911	-7%	13050	12050	-8%
AW5	F_d (kN)	3606	4030	12%	5697	6547	15%	7709	8695	13%
	δ_{max} (mm)	231	211	-9%	169	172	1%	127	152	19%
	F_1 (kN)	10372	10968	6%	9719	10911	12%	11191	12050	8%
AW6	F_d (kN)	4249	4030	-5%	7488	6547	-13%	9298	8695	-6%
	δ_{max} (mm)	241	211	-12%	197	172	-13%	159	152	-4%
	F_1 (kN)	11377	10968	-4%	12289	10911	-11%	12900	12050	-7%
AW7	F_d (kN)	4149	4030	-3%	6402	6547	2%	8156	8695	7%
	δ_{max} (mm)	197	211	7%	151	172	13%	138	152	10%
	F_1 (kN)	9891	10968	11%	10265	10911	6%	11680	12050	3%

Figure 7 shows the response of isolation system displacement coefficient (R_D) about added damping ratio (ζ_d). With ζ_d increasing, R_D presents a monotonic decrease, and the decay rate gradually slows. The R_D presents the most sensitive decrease in the ζ_d range of 0–0.4, i.e., damping has the most influence on reducing the displacement in this ζ_d range. Beyond this range, the effectiveness of displacement reduction weakens considerably, and the curve flattens—suggesting a progressive saturation of the damping effect.

This result shows an obvious "efficiency boundary". The theoretical curve accurately captures this nonlinear behavior, confirming its suitability for characterizing the attenuation of isolation system displacement.

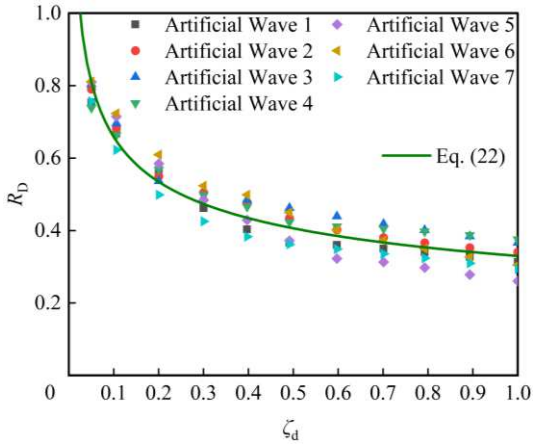


Figure 7. Displacement coefficient versus damping ratio.

Unlike the displacement coefficient, the total shear coefficient R_V in Fig. 8 is a non-monotonic function of increasing added damping ratio ζ_d at first decreasing rapidly and then increasing. This behavior reveals the existence of an optimal added damping ratio that minimizes the shear coefficient. Such a trend arises from the dual role of damping in structural response. On the one hand, additional damping dissipates seismic energy and suppresses isolator displacement, thereby reducing the base shear. On the other hand, excessive damping alters the dynamic properties of the isolation layer, which may amplify the high-frequency components of ground motion and trigger a subsequent rise in base shear. The theoretical formulation is able to accurately capture this extremum and reveal the underlying competition between energy dissipation and shear amplification.

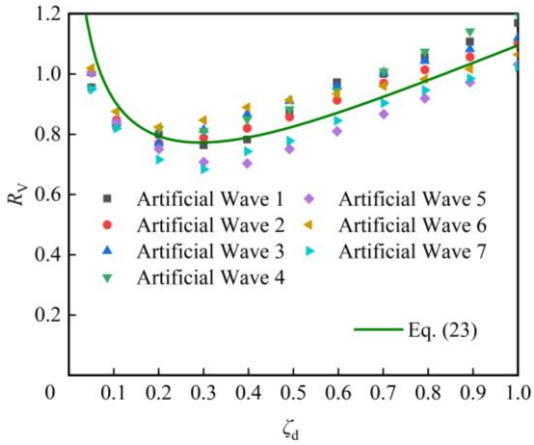


Figure 8. Total shear coefficient versus damping ratio.

In total, the theoretical model could be used to predict the displacement and shear responses under MCE accurately. Moreover, the attenuation characteristic of the damping efficiency for the displacement control and the intrinsic mechanism for the optimal damping ratio for shear control could be revealed. These results are of important guidance for the efficient and safe seismic isolation design.

3 Multi-objective optimization of hybrid isolation systems

3.1 Optimum shear design

A key design objective is to minimize the total shear in the isolation layer, which concurrently minimizes structural acceleration and inter-story forces [58]. The added damping ratio ζ_d^* that achieves this minimum, $\alpha_{1\min}$, is derived by setting the derivative of Eq. (23) with respect to ζ_d to zero, yielding the analytical solution

$$\zeta_d^* = \sqrt{\frac{3C}{7D}} \qquad (24)$$

Substituting Eq. (24) into Eq. (23) yields the minimum shear response ratio $R_{v,\min}$, given by

$$R_{v,\min} = \frac{\alpha_{1,\min}}{\alpha_0} = 1.357C^{0.35}D^{0.15} \qquad (25)$$

Substituting Eq. (24) into Eq. (22) gives the displacement response ratio R_D,$\alpha_{1\min}$ corresponding to the minimum total shear coefficient $\alpha_{1,\min}$

$$R_{D,\alpha 1\min} = \frac{\delta_{\max,\alpha 1\min}}{\delta_0} = B\left(\frac{7D}{3C}\right)^{0.15} \qquad (26)$$

Substituting the optimal damping ratio ζ_d^* from Eq. (24) into Eq. (20) gives the corresponding damping parameter at minimum shear force

$$\alpha_{d,\alpha 1\min} = \alpha_0 A(\frac{3C}{7D})^{0.35} \qquad (27)$$

Here, $\delta_{\max,\alpha 1\min}$ denotes the maximum displacement of the isolation layer corresponding to $\alpha_{1,\min}$. Accordingly, the maximum feasible shear force reduction provided by viscous dampers can be reasonably estimated, given the earthquake input energy (quantified by velocity V_E) and the parameters of isolation bearings. Subsequently, the corresponding maximum shear force and displacement of the isolation layer, as well as the predicted maximum damping force, can be determined via Equations (25), (26) and (27).

3.2 Weighted optimization of displacement and shear design

The optimal shear design that minimizes the total shear coefficient of the isolation layer fails to fully consider the isolation layer displacement demand. Adopting the same strategy for determining the added damping ratio via response ratio function minimization, this section presents an optimal design method to identify damper damping parameters based on user-specified tradeoffs between displacement and shear demands. A weighted objective function Δ is defined as a linear combination of the displacement response ratio R_D and the shear response ratio R_V.

$$\Delta = \min R = \min\ (aR_D + bR_V) \qquad (28)$$

where R denotes the combined response function, and a and b represent the weighting coefficients for displacement and shear, respectively, with $a+b=1$.

Substituting Eqs. (22) and (23) into Eq. (28) yields the linear combination function R

$$R = a\mathrm{B}\zeta_d^{-0.3} + b\sqrt{C\zeta_d^{-0.6} + D\zeta_d^{1.4}} \qquad (29)$$

A minimum of the function R defined in Eq. (29) exists only if $b \neq 0$. Taking the derivative of Eq. (29) and setting it to zero yields the added damping ratio $\zeta_{d,\Delta}$ that minimizes R

$$\zeta_{d,\Delta} = \sqrt{\frac{42b^2C + 9a^2B^2 + 3aB\sqrt{280b^2C + 9a^2B^2}}{98b^2D}} \quad (30)$$

Substituting Equation (30) into Equations (20), (22), and (23) yields the damping $\alpha_{d,\Delta}$ at which R attains its minimum, together with the total shear response ratio $R_{V,\Delta}$ and the displacement response ratio $R_{A,\Delta}$. Once the weighting coefficients a and b are determined, the optimal damping ratio $\zeta_{d,\Delta}$ can be directly obtained from Equation (30). The corresponding optimal damping coefficient is then given by $C_\Delta = 4\pi M\zeta_d / T_f$.

In practice, the weighting coefficients a and b should be selected based on the relative emphasis placed on isolation-layer displacement versus shear force in the optimization. Five representative combinations corresponding to shear weighting coefficients of b=0, 0.35, 0.5, 0.75, and 1.0 are listed in Table 2, along with their respective optimization objectives. The corresponding linear combination function R curves for these five scenarios are plotted in Figure 9. When b=1, the function reduces to $R = R_V = \alpha_1 / \alpha_0$, and the optimal damping $\alpha_{d,\Delta}$ coincides with that required for optimal shear design, denoted as $\alpha_{d,\alpha 1min}$. As b decreases, the R curve flattens and gradually shifts toward δ_{max} / δ_0. Correspondingly, the extremum point shifts rightward, implying a rise in the optimal added damping ratio. For b = 0, the function reduces to R=$R_D = \delta_{max}/\delta_0$, which decays monotonically and exhibits no extremum. This case corresponds to a design criterion based solely on isolation-layer displacement, where the required added damping ratio of the viscous dampers should be determined from Equation (22) according to the permissible displacement.

Table 2. Optimization objectives under various weighting combinations.

Combination	Weight a	Weight b	Optimization objective
1	0	1. 0	Shear force only
2	0.25	0.75	Both shear force and displacement, with emphasis on shear force
3	0.5	0.5	Both shear force and displacement
4	0.65	0.35	Both shear force and displacement, with emphasis on displacement
5	1	0	Displacement only

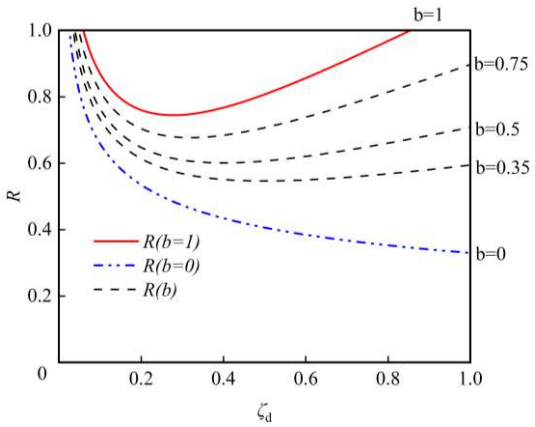


Figure 9. Function R versus weighting combinations.

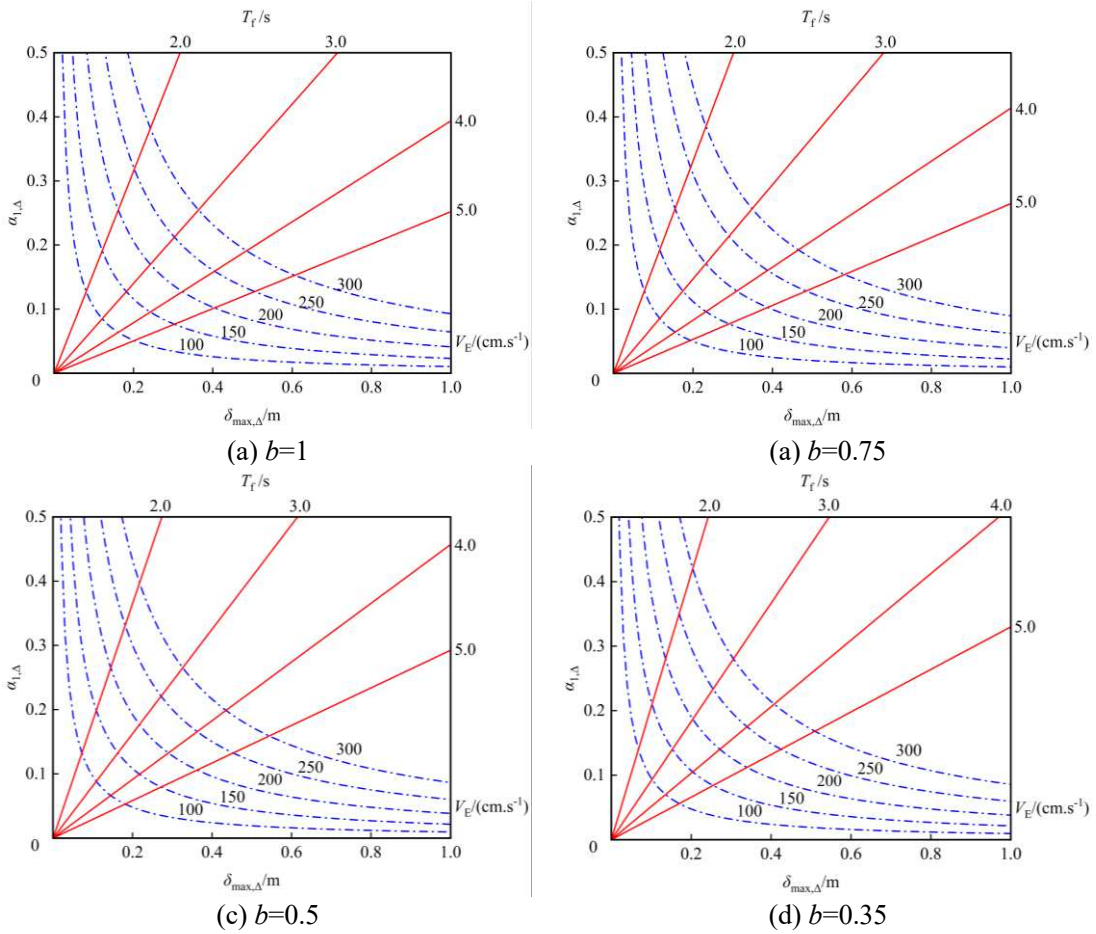
Under an optimal design, the relationship between the total shear coefficient $\alpha_{1,\Delta}$ of the isolation layer and the maximum displacement $\delta_{\max,\Delta}$ can be formulated in terms of the fundamental period $T_{\mathrm{f},300}$

$$\alpha_{1,\Delta} == \alpha_0 R_{\mathrm{V},\Delta} = \frac{\delta_0\sqrt{8\pi^3 n_\mathrm{b}\varsigma_{\mathrm{eq},300}}}{T_{\mathrm{f},300}}\frac{1}{T_{\mathrm{f},300}g}\sqrt{\frac{2\pi}{n_\mathrm{b}\varsigma_{\mathrm{eq},300}}}R_{\mathrm{V},\Delta} = \frac{4\pi^2\delta_{\max,\Delta}}{gT_{\mathrm{f},300}^2}\frac{R_{\mathrm{V},\Delta}}{R_{\mathrm{D},\Delta}} \quad (31)$$

Alternatively, the same relationship can be expressed using the energy spectrum V_E

$$\alpha_{1,\Delta} = \frac{V_\mathrm{E}^2}{2\pi n_\mathrm{b} g\varsigma_{\mathrm{eq},300}\delta_{\max,\Delta}}R_{\mathrm{V},\Delta}R_{\mathrm{D},\Delta} \quad (32)$$

Based on Equations (31) and (32), the relationships between $\alpha_{1,\Delta}$ and $\delta_{\max,\Delta}$ for the four representative combinations (Combinations 1 through 4 in Table 2) are presented in Figure 10, with the fundamental period T_f and the energy spectrum V_E as the design parameters. This figure enables quick estimation of the isolation layer responses under the four optimization schemes.



(a) b=1 (a) b=0.75

(c) b=0.5 (d) b=0.35

Figure 10. Relationship of the optimized total shear coefficient to the maximum displacement.

3.3 Optimized design workflow

On the basis of the aforementioned design principles, an optimal design procedure for installing viscous dampers in the isolation layer of isolated structures is proposed, as depicted in Fig. 11. Given the predetermined design parameters of the superstructure, the optimal design procedure comprises the subsequent steps:

(1) Bearing Layout Determination

Based on the superstructure loads and column grid layout, the tributary area is determined to establish the bearing diameter. The appropriate bearing type is then selected, from which the fundamental period of the isolated structure, T_f, is subsequently obtained.

(2) Ground Motion Selection

Ground motions are selected based on site conditions and structural dynamic parameters. Subsequently, the equivalent velocity of seismic input energy V_E and the number of hysteretic cycles n_b are determined.

(3) Calculation of Reference Response Quantities

The reference displacement of the isolation layer δ_0 is calculated via Equation (8), and the reference shear coefficient α_0 is calculated via Equation (9).

(4) Determination of Weighting Coefficients

Based on the optimization objectives, the weighting coefficients a and b are selected, and the optimal added damping ratio is calculated using Equation (30).

(5) Seismic Response Prediction

The predicted displacement of the isolation layer ($\delta_{max,\Delta}$) is determined using Equations (22). The shear force of the isolation layer (F_1) is derived from Equations (4) and (23). The damper force (F_d) is computed via Equations (4) and (20). For structures with a fundamental period $T_f \leq 5$ s, the shear force and displacement responses of the isolation layer can be supplemented by approximate estimates from Figure 10.

(6) Assessment of Conformance to Design Performance Requirements

The predicted responses are compared against the performance targets. If both the displacement and shear force requirements are satisfied, the optimal damping coefficient is calculated as $C_\Delta = 4\pi M\zeta_{d,\Delta}/T_f$. If the displacement requirement is not met, the procedure reverts to Step 4 with a decreased shear weighting coefficient b. In contrast, if the total shear force requirement is not satisfied, the procedure reverts to Step 4 with an increased shear weighting coefficient b.

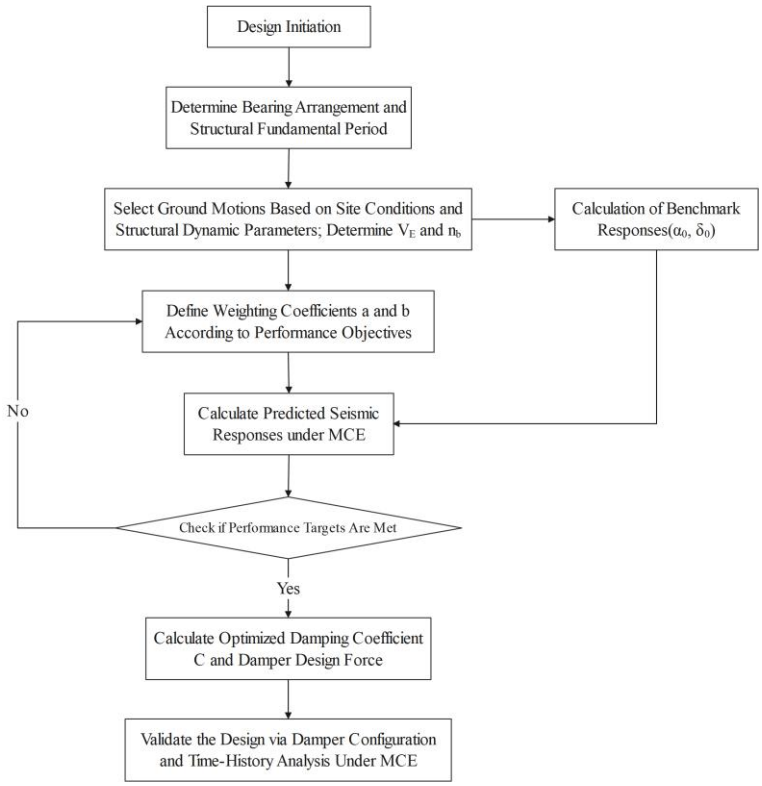


Figure 11. Flowchart for the optimized design of supplemental viscous dampers in isolated structures.

4 Theoretical validation and design case analysis

To verify the effectiveness and accuracy of the proposed response prediction theory and multi-objective optimization design method, a seven-story frame structure in Kashi, Xinjiang, is selected as the engineering case. A case study is conducted on the optimal design of additional viscous dampers in the isolation layer and the associated seismic response analysis.

4.1 Project overview and bearing selection

This study is based on a seven-story frame structure located in Kashi Prefecture, Xinjiang Uygur Autonomous Region. The building functions as Teaching Building No. 3 and is designated as a key fortification category structure. The seismic fortification intensity is 8, and the design basic acceleration is 0.30 g. The site condition is Category II, Seismic Group 3. The characteristic period is 0.5 s. The geotechnical investigation results excluded the possibility of near-fault conditions. The isolation layer is placed on top of the foundation. The superstructure is a seven-story reinforced concrete frame structure. The typical story height is 3.3 m, resulting in a total structural height of 23.1 m. The building plan width is 17.0 m, giving a height-to-width ratio of 1.4. In highly seismic regions, conventional seismic design leads to the following problems: excessively large column cross-sections, significant reduction in usable floor space, and difficulty in meeting the higher performance requirements expected for key protected structures. To address these issues, this study uses the optimization flow chart shown in Figure 11 to optimize the design of additional viscous dampers in the isolation layer under MCE.

Bearing selection follows Article 4.6.3 of the Standard for Seismic Isolation Design of Buildings (GB/T 51408-2021). Article 4.6.3 specifies that the compressive stress of bearings shall not exceed 12 MPa under the representative gravity load for key fortification category structures. According to the column layout and corresponding tributary area, the maximum axial load at the column base is 5600 kN. Therefore, bearings with a diameter of 800 mm are adopted, and LRB800 lead-rubber bearings are selected. Their

mechanical properties are listed in Table 3. Using the selected isolator parameters, the fundamental period of the isolated structure is obtained as $T_f = 3.72$ s, with a total mass of the superstructure $M = 7470$ t. These parameters provide the basis for subsequent ground motion selection and reference response quantity calculation.

Table 3. Parameters of the seismic isolation bearings.

Bearing Type	Quantity	Vertical Stiffness (kN/mm)	Pre-yield Stiffness (kN/mm)	Post-yield Stiffness (kN/mm)	Yield Force（kN）	Equivalent Horizontal Stiffness (100%) (kN/mm)	Equivalent Horizontal Stiffness (300%) (kN/mm)	Equivalent Damping Ratio	Total Rubber Thickness (mm)
LRB800	18	2500	14.3	1.08	106	1.8	1.2	0.16	150

4.2 Selection of ground motion time histories for maximum considered earthquakes

This study implements Clause 4.1.3 of GB/T 51436-2021 and Clause 5.1.2 of GB 50011-2010 for seismic input control [43, 59]. Ground motion selection follows tripartite criterion, intensity, spectral characteristics, duration. In line with these criteria, we selected five recorded ground motions and two artificially generated ground motions for time-history analysis. Detailed information for each selected ground motion is presented in Table 4, and the time history curves are shown in Fig. 12.

Table 4. Ground motion record information.

Record ID	Natural Record Name	Station Name	PGA (cm/s²)	PGV (cm/s)	Fault Distance (km)	Peak Acceleration for MCE (cm/s²)	Time Step	Number of Data Points
R1	/	/	/	/	/	510	0.02	1501
R2	/	/	/	/	/	510	0.02	1501
T1	Chi-Chi, Taiwan-03_NO_2457	CHY024	276.2	50.7	9.3	510	0.005	10999
T2	TH3TG065	TCU065	767	145	0.4	510	0.02	2001
T3	Imperial Valley-06_NO_170	EC County Center FF	176.4	54.47	14.9	510	0.005	7997
T4	Kocaeli, Turkey_NO_1163	Yarimca Petkim	315.7	67.0	4.8	510	0.005	20323
T5	Loma Prieta_NO_737	Gilroy Array #3	485	32.45	9.64	510	0.005	8000

Note 1: All ground motions (natural and artificial) were normalized to a peak acceleration of 510 cm/s², corresponding to the intensity of the Maximum Considered Earthquake (MCE) for the site, to ensure consistent input intensity.

Note 2: The records were selected to match the characteristic site period (Tg) of the project site, ensuring compatibility of spectral characteristics.

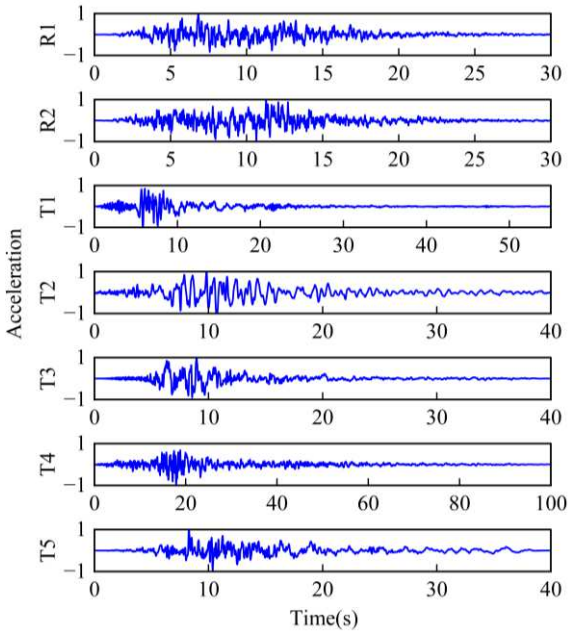


Figure 12. Time history curves of normalized, dimensionless acceleration.

Structural base shears were calculated through time-history analysis and response spectrum methods (Table 5). Results from individual waves exceeded 65% of response spectrum values, while the seven-wave ensemble average surpassed 80% of spectrum-based calculations. These outcomes meet the upper and lower base shear limits specified in GB 50011-2010 Clause 5.1.7 [59], validating the reliability and analytical validity of strength evaluation.

Table 5. Base shear.

Load case		Response spectrum	R1	R2	T1	T2	T3	T4	T5	Mean time-history response
Base shear (kN)	X	13622	16518	14946	15042	13340	13538	13179	14544	14444
	Y	13478	16494	14929	15023	13037	13493	13245	14408	14376
percentage (%)	X	100	121	110	110	98	99	97	107	106
	Y	100	122	111	111	97	100	98	107	107

Note: Percentage represents ratios of base shear from time-history analyses to those derived via the modal response spectrum method.

The duration of each wave, measured as the time interval between the first and last occurrence of 10% of the peak acceleration, varies from 5.69 to 14.45 times the fundamental period (see Table 6). This range partially meets the requirement of 5 to 10 times the fundamental period specified in GB 50011-2010 [59] Clause 5.1.7. Duration coverage allows the structural response and energy dissipation process to be captured accurately, which prevents the overall damage from being underestimated by short-duration ground motions.

Table 6. Duration parameters of seven selected time history spectra.

Time-History record	First arrival time at 10% of peak acceleration (s)	Last occurrence time at 10% of peak acceleration (s)	Effective duration (s)	Fundamental period (s)	Ratio

R1	2.33	24.16	21.83	3.72	5.87
R2	2.07	24.02	21.96	3.72	5.90
T1	1.21	24.31	23.09	3.72	6.21
T2	1.31	35.54	34.23	3.72	9.20
T3	3.59	24.78	21.19	3.72	5.69
T4	2.68	56.44	53.76	3.72	14.45
T5	4.18	36.34	32.16	3.72	8.65

Fig. 13 and Table 7 show the 7-wave average seismic influence coefficient curve compared with the code-specified response spectrum at fundamental periods. The maximum percentage deviation at the control period is 10.7%, which is much smaller than the 20% limit required by GB 50011-2010 Clause 5.1.7 [59]. Good spectral matching between input motions and the design spectrum is ensured by this spectral consistency.

Table 7. Comparison of influence coefficients for seven time history response spectra and code response spectrum.

Mode shape order	Fundamental period (s)	Seismic influence coefficient (α)		Difference (%)
		Time-history method	Code spectrum method	
1	3.72	0.202	0.197	2.4%
2	3.70	0.203	0.198	2.3%
3	3.35	0.226	0.217	4.2%

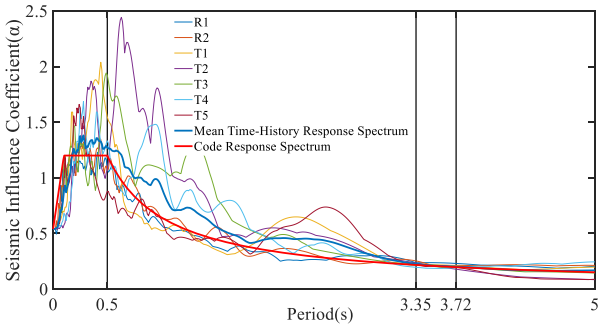


Figure 13. Comparison of seven time history response spectra and code response spectrum. (α_{max}=1.2, T_g=0.50 s)

In conclusion, the seven selected ground motions meet the requirements of GB 50011-2010 [59] in terms of intensity, duration, and spectral matching. Such compliance provides reasonable assurance for the subsequent time-history analysis.

4.3 Energy-based seismic response quantities and optimization objectives

Based on the ground motion selection results in Section 4.2, the velocity-equivalent under MCE is determined as V_E=175 cm/s, and the equivalent number of hysteretic cycles for the lead-rubber bearings is n_b=3.5. Substituting these parameters into Eqs. (8) and (9) yields a reference isolation displacement δ_0 =

550 mm and a reference shear coefficient α_0 = 0.17. These reference response quantities serve as the baseline for the subsequent optimization of dampers.

In this study, the optimization objective is defined to balance the control of isolation layer displacement and total shear force, with priority given to base shear force control. Accordingly, the weighting coefficients are set as a = 0.25 for displacement and b = 0.75 for shear. Substituting these coefficients into Eq. (30) yields an optimal added damping ratio of $\zeta_{d,\Delta}$= 0.34. From Eqs. (22) and (23), the response ratios are obtained as $R_{D,\Delta}$=0.46 for isolation displacement and $R_{V,\Delta}$=0.77 for total shear. Based on the reference responses, the predicted maximum isolation displacement under the optimal design is $\delta_{max,\Delta}=\delta_0 R_{D,\Delta}$=253 mm, and the predicted total shear is $F_{1,\Delta}=Mg\alpha_0 R_{V,\Delta}$ = 9778 KN.

The calculated maximum displacement $\delta_{max,\Delta}$ is 253 mm, which satisfies the limit min (0.55D, 3Σtr) specified in Clause 4.6.6 of GB/T 51408-2021 [43]. This limit governs bearing displacement under MCE, where D and Σtr represent the bearing diameter and total rubber thickness, respectively. Additionally, the isolation layer yields a shear force response ratio $R_{V,\Delta}$ of 0.77, which represents a 23% decrease in shear relative to the structure installed with sole isolation bearings. The result meets the predefined seismic performance objective.

4.4 Viscous damper parameter design based on optimal damping ratio

According to the optimized added damping ratio $\zeta_{d,\Delta}$=0.34 obtained in Section 4.3, the parameters of viscous damper are designed. Taking into account $C_\Delta=4\pi M\zeta_{d,\Delta}/T_f$, the damping coefficient is calculated as C_Δ=9938 kN·s/m. Subsequently, according to Equations (4), (9), and (20), the maximum damper output force is calculated as F_d=5715 kN.

When the design force of a single viscous damper exceeds 2000 kN, the complexity of connector detailing, embedded component design, and long-term maintainability rises significantly, while its economic efficiency and constructability deteriorate in practice [60]. In response, and guided by the principle of "uniform, dispersed, symmetric, and peripheral" layout, this project adopts four viscous dampers in each primary direction, with a controlled design force of 1600 kN per damper. The corresponding layout and design parameters are illustrated in Figure 14 and summarized in Table 8, respectively.

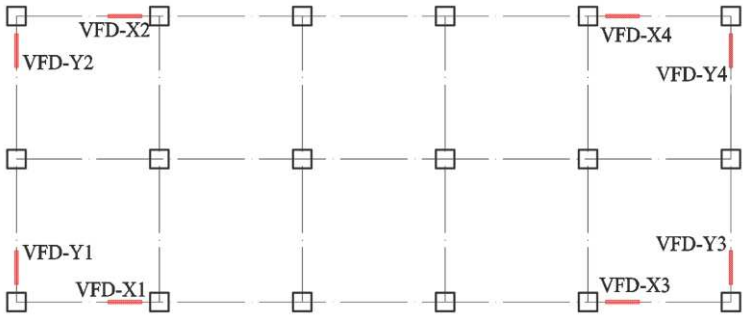


Figure 14. Layout plan of dampers in seismic isolation layer.

Table 8. Damper parameters.

Damper	Quantity	Damping coefficient, C (kN · s·m^{-1})	Design force (kN)
X-Damp	4	2500	1600
Y-Damp	4	2500	1600

Damping parameters obtained from the design will be incorporated into the time-history analysis model to evaluate the seismic mitigation performance of the optimized scheme.

4.5 Verification of optimized design using time-history analysis

To fully validate the effectiveness of the proposed method, a comparative analysis is conducted from three perspectives. These include the performance enhancement achieved with the addition of dampers, the variation in structural response under different optimization objectives, and the accuracy of theoretical predictions relative to the results obtained from time-history analysis.

Table 9 compares the seismic responses of the isolated system with and without the optimized dampers. Without dampers, the mean isolation layer displacement reaches 530 mm, exceeding the code-specified limit, and noticeable acceleration responses are observed at both the first and top floors. Upon installation of the optimized dampers, the mean displacement reduces to 278 mm, complying with the code requirement. The acceleration reductions at the first and top floors are 19% and 6%, respectively. Figure 15 plots the time-history curves of isolation layer displacement under the T2 ground motion. It reveals that the dampers not only remarkably mitigate the peak displacement but also maintain stable energy dissipation throughout the excitation duration.

Table 9. Structural response under optimal design.

Case	Isolation layer displacement (mm)	Bottom shear ratio	First-story acceleration (m/s²)	Top story inter-story displacement (mm)	Top story acceleration (m/s²)
Without dampers	530	0.165	2.81	5.1	4.16
With dampers	278	0.147	2.36	4.8	3.45

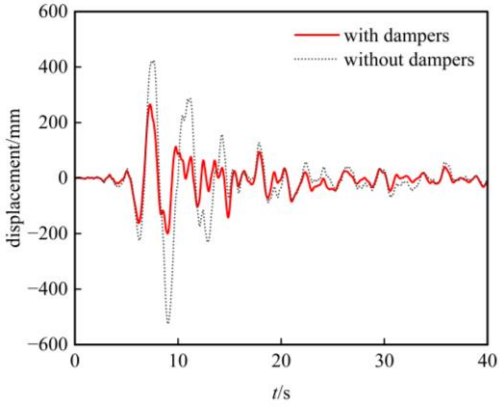


Figure 15. Time-history response of isolation layer displacement.

Optimization designs based on the four weighting coefficient combinations (Combinations 1-4) presented in Table 2 were carried out and then time-history analyses were conducted; the related results are listed in Tables 10 and 11. In comparison with the benchmark responses, the isolation layer displacement and total shear force decrease significantly for all four optimization schemes. Among them, Combination 1 (b = 1.0) yielded the optimal shear force design, with the time-history total shear coefficient approaching the minimum of the theoretical prediction curve. With the shear weighting coefficient b decreasing and the displacement weighting coefficient a increasing, the optimal damping ratio increases gradually. The time-history analysis responses presented a similar trend of decreasing displacement and increasing total shear

force, which matched well with the objectives of optimization presented in Table 2. These findings validate that the proposed multi-objective optimization method effectively reflects the varying priorities of designers.

Table 10. Optimized damping parameters for different combinations.

Parameters	Combination 1 (a=0, b=1)	Combination 2 (a=0.25, b=0.75)	Combination 3 (a=0.5, b=0.5)	Combination 4 (a=65, b=0.35)
$\zeta_{d,\Delta}$	0.29	0.34	0.42	0.53
C/(kN·s) · m^{-1}	8476	9938	12276	15491
F_d/(kN)	5274	5936	6722	8046

Table 11. Comparison of key responses under MCE for different combinations.

Key responses under MCE	Combination 1 (a=0, b=1)			Combination 2 (a=0.25, b=0.75)			Combination 3 (a=0.5, b=0.5)			Combination 4 (a=0.65, b=0.35)		
	Time-history average	Predicted value	Difference (%)	Time-history average	Predicted value	Difference (%)	Time-history average	Predicted value	Difference (%)	Time-history average	Predicted value	Difference (%)
$F_{d,\Delta}$/(kN)	5274	5082	4%	5936	5715	4%	6722	6587	2%	8046	7752	4%
$\delta_{max,\Delta}$/(mm)	301	265	12%	280	253	10%	257	236	8%	229	220	4%
$F_{1,\Delta}$/(kN)	10639	9754	8%	11106	9778	12%	111664	10011	14%	12773	10538	17%

Table 11 compares the theoretical predictions with the mean values from time-history analyses for isolation layer displacement, total shear force, and damper force under the four optimization schemes. The maximum deviations are 12% for displacement, 17% for total shear and 4% for damper force, all within acceptable engineering limits. The favorable agreement between the theoretical curves and the scattered data points from time-history analyses (Figs. 6-8) further validates the reliability of the proposed predictive formulae.

In summary, this section validates the accuracy of the response prediction formulas presented in Section 2 and the feasibility of the multi-objective optimization design method proposed in Section 3 using a practical engineering case. Time-history analysis results demonstrate that the response indices of the hybrid isolation system optimized via the proposed method agree well with the theoretical predictions. This validates that the theoretical framework is reliable and efficient for engineering design practice.

5 Conclusions

This study derives a response prediction theory for hybrid isolation systems and proposes a multi-objective optimization design methodology that enables coordinated control of displacement and shear force. The main findings are summarized as follows.

(1) Based on an energy balance derivation, a response prediction formula is proposed that establishes an explicit mapping from the added damping ratio ζ_d to the isolation displacement response ratio R_D and the total shear response ratio R_V. The formula reveals that the reduction in R_D diminishes as ζ_d increases, along with a non-monotonic trend in R_V, which first decreases and then increases—confirming the existence of an "optimal damping ratio". Time-history analysis validation demonstrates that the prediction errors for displacement and total shear are within 12% and 17%, respectively, which meets the accuracy requirements for preliminary engineering design.

(2) Time history analysis is performed to calibrate the key energy parameters of the hybrid isolation system, and a power-law relationship is formulated between damping force and added damping ratio (ζ_d).

This relationship effectively captures the nonlinear dependence between the two under seismic excitation, enabling direct estimation of damper parameters without complex iterative calculations.

(3) A multi-objective optimization method is proposed by integrating displacement control and shear force control into a unified framework via a linear weighted sum function. Designers can adjust the weighting coefficients based on practical engineering requirements, and the optimal added damping ratio is directly derived via a closed-form solution. Subsequently, both seismic response evaluations and the corresponding damper parameters can be explicitly calculated. This method eliminates the iterative trial-and-error process commonly required in time history analysis, thus significantly enhancing design efficiency.

(4) Case studies demonstrate that for various weighting combinations, the response trends obtained from time-history analysis closely match theoretical predictions, confirming that the optimization method effectively reflects the designer's relative emphasis on displacement versus shear force control. The proposed method is primarily intended for low-to-medium-rise base-isolated structures; its applicability to more complex scenarios—such as those involving notable higher-mode effects or nonlinear viscous dampers—requires further investigation.

Overall, this study establishes a theoretical basis and provides a practical tool for the preliminary design and parameter optimization of hybrid isolation systems. The proposed approach significantly reduces iterative design costs while maintaining acceptable accuracy, offering both theoretical innovation and strong potential for engineering application.

Funding: This research was funded by the Introduction of Talent Research Initiation Fund of Kashi University (No. GCC2024ZK-018), the Open project of Xinjiang Key Laboratory of Engineering Materials and Structural Safety (No. XKLEMSS2025B06) and the College Students' Innovation and Entrepreneurship Training Program (No. 202510763147). The authors are very grateful for this support. Any opinions, findings, and conclusions or recommendations expressed in this material are those of the authors and do not necessarily reflect the views of the fundings.

Data Availability Statement: The original contributions presented in the study are included in the article, further inquiries can be directed to the corresponding author.

Acknowledgments: In particular, the author would like to thank the editor for the careful editing and layout of this article, as well as the reviewer for their valuable comments and suggestions for this article.

Disclosure statement

No potential conflict of interest was reported by the authors.

References

[1] Dalal Sejal P, Vasanwala S A, Desai A K. Performance based seismic design of structure: A review[J]. International Journal of Civil and Structural Engineering, 2011, 1(4): 795-803.

[2] Horton T A, Hajirasouliha I, Davison B, et al. More efficient design of reduced beam sections (RBS) for maximum seismic performance[J]. Journal of Constructional Steel Research, 2021, 183: 106728.

[3] Su N, Qin L, Zeng C, et al. Multi-modal multi-response seismic mitigation with amplified inerter

negative stiffness dampers[J]. International Journal of Mechanical Sciences, 2025, 301: 110516.

[4] Xiang, N.L.; Li, J.Z. Experimental and numerical study on seismic sliding mechanism of laminated-rubber bearings. Eng. Struct. 2017, 141, 159 – 174.

[5] Derham, C.J.; Kelly, J.M.; Thomas, A.G. Nonlinear natural rubber bearings for seismic isolation. Nucl. Eng. Des. 1985, 84, 417 – 428.

[6] Wada, A.; Kani, N.; Hirano, S.; Kamikouchi, H.; Kimura, M. Seismic isolated structures applied to from detached houses to high-rise apartments in Japan. In Proceedings of the 5th International Conference on Urban Earthquake Engineering, Tokyo, Japan, 4 – 5 March 2008.

[7] Losanno D, Sierra I E M, Spizzuoco M, et al. Experimental assessment and analytical modeling of novel fiber-reinforced isolators in unbounded configuration[J]. Composite Structures, 2019, 212: 66-82.

[8] Chen P, Wang B, Dai K, et al. Analytical and numerical investigations of base isolation system with negative stiffness devices[J]. Engineering Structures, 2022, 268: 114799.

[9] Das S, Gur S, Mishra S K, et al. Optimal performance of base isolated building considering limitation on excessive isolator displacement[J]. Structure and Infrastructure Engineering, 2015, 11(7): 904-917.

[10] Abdeddaim M, Djerouni S, Ounis A, et al. Optimal design of Magnetorheological damper for seismic response reduction of Base-Isolated structures considering Soil-Structure interaction[C]//Structures. Elsevier, 2022, 38: 733-752.

[11] Wang H, Shen W, Zhu H, et al. Stochastic optimization of a nonlinear base isolation system with LRB and EIMD for building structures[J]. Structural Control and Health Monitoring, 2023, 2023(1): 8392421.

[12] Deringöl A H, Güneyisi E M, Hansu O. Combined effect of bearing stiffness of the base isolator and damping characteristics of the viscous damper on the nonlinear response of buildings[J]. International Journal of Steel Structures, 2022, 22(5): 1497-1517.

[13] Liu, Y.; Wu, J.; Donà, M. Effectiveness of fluid-viscous dampers for improved seismic performance of inter-storey isolated buildings. Eng. Struct. 2018, 169, 276 – 292. [CrossRef]

[14] Avossa, A.M.; Pianese, G. Damping Effect on the Seismic Response of Base-Isolated Structures with LRB Devices. Ing. Sismica 2017, 34, 3 – 30.

[15] Kelly, J.M. The role of damping in seismic isolation. Earthq. Eng. Struct. Dyn. 1999, 28, 3 – 20

[16] Naeim F, Kelly J M. Design of seismic isolated structures: from theory to practice[M]. John Wiley & Sons, 1999.

[17] Makris N. Seismic isolation: Early history[J]. Earthquake Engineering & Structural Dynamics, 2019,

48(2): 269-283.

[18] Makris N, Chang S P. Effect of damping mechanisms on the response of seismically isolated structures[R]. Berkeley, CA, USA: Pacific Earthquake Engineering Research Center, 1998.

[19] Kitayama S, Constantinou M C. Performance evaluation of seismically isolated buildings near active faults[J]. Earthquake Engineering & Structural Dynamics, 2022, 51(5): 1017-1037.

[20] Kitayama S, Constantinou M C. Collapse performance of seismically isolated buildings designed by the procedures of ASCE/SEI 7[J]. Engineering Structures, 2018, 164: 243-258.

[21] De Domenico D, Ricciardi G. Improved stochastic linearization technique for structures with nonlinear viscous dampers[J]. Soil Dynamics and Earthquake Engineering, 2018, 113: 415-419.

[22] De Domenico D, Ricciardi G. Earthquake protection of structures with nonlinear viscous dampers optimized through an energy-based stochastic approach[J]. Engineering Structures, 2019, 179: 523-539.

[23] Yun hao Z, Bo L, Guo qian Y. Seismic response prediction and optimization design method for base isolated structure based on energy balance[J]. Journal of Vibration and shock,2021,40(17):32-40.DOI:10.13465/j.cnki.jvs.2021.17.005.

[24] Ozer E, Inel M. The effect of single and combined use of base isolator and fluid viscous damper on seismic performance in a conventional RC building with torsional irregularity[J]. Journal of Building Engineering, 2025, 101: 111898.

[25] Liu X, Wang W, Li J. Full-scale shaking table tests and numerical studies of structural frames with a hybrid isolation system[J]. Engineering Structures, 2023, 292: 116545.

[26] WANG Wei, LIU Xiaotian. Shaking table test on hybrid isolation system of prefabricated industrial equipment supports[J]. Journal of Building Structures, 2023, 44(10): 15-25. https://doi.org/10.14006/j.jzjgxb.2022.0315

[27] Habieb A B, Milani G, Tavio T. Two-step advanced numerical approach for the design of low-cost unbonded fiber reinforced elastomeric seismic isolation systems in new masonry buildings[J]. Engineering Failure Analysis, 2018, 90: 380-396.

[28] Deringöl A H, Güneyisi E M, Hansu O. Combined effect of bearing stiffness of the base isolator and damping characteristics of the viscous damper on the nonlinear response of buildings[J]. International Journal of Steel Structures, 2022, 22(5): 1497-1517.

[29] Qiao Yun W,Zi liang L.Effect of Mid-Story Isolation Layer Location Variation on the Control Effectiveness of Hybrid Passive Control Systems: An Experimental Study[J].Journal of Vibration

677 Engineering,2022,35(01):1-12.DOI:10.16385/j.cnki.issn.1004-4523.2022.01.001.
678 [30] Chun Xiang L, Qiu Yu L. Performance-Oriented Optimal Design of Hybrid Base Isolation
679 Systems[J].Journal of Vibration Engineering,2024,37(01):137-147.DOI:10.16385/j.cnki.issn.1004-
680 4523.2024.01.014.
681 [31] Alwilly G, Lavan O. Optimal Seismic Design of Multiple Isolation Systems and Viscous Dampers in
682 Vertically Irregular Frame Buildings[J]. Earthquake Engineering & Structural Dynamics, 2026, 55(1): 150-
683 168.
684 [32] Charmpis D C, Komodromos P, Phocas M C. Optimized earthquake response of multi‐storey
685 buildings with seismic isolation at various elevations[J]. Earthquake Engineering & Structural Dynamics,
686 2012, 41(15): 2289-2310.
687 [33] Öncü-Davas S, Temür R, Alhan C. Comparison of meta-heuristic approaches for the optimization of
688 non-linear base-isolation systems considering the influence of superstructure flexibility[J]. Engineering
689 Structures, 2022, 263: 114347.
690 [34] Skandalos K, Afshari H, Hare W, et al. Multi-objective optimization of inter-story isolated buildings
691 using metaheuristic and derivative-free algorithms[J]. Soil Dynamics and Earthquake Engineering, 2020,
692 132: 106058.
693 [35] Bernardi E, Donà M, Tan P. Multi-objective optimization of the inter-story isolation system used as a
694 structural TMD[J]. Bulletin of Earthquake Engineering, 2023, 21(5): 3041-3065.
695 [36] Li T, Liu R, Sun G, et al. Seismic Performance of High-Rise Shear Walls with Hybrid Control: Sparse
696 Isolation Bearings and Viscous Fluid Dampers[J]. Buildings, 2026, 16(1): 208.
697 [37] Leblouba M. Selection of seismic isolation system parameters for the near-optimal design of
698 structures[J]. Scientific Reports, 2022, 12(1): 14734.
699 [38] Li C, Zhao J, Pan H, et al. Deep reinforcement learning based performance optimization of hybrid
700 system for base-isolated
701 [39] Qian X, Sato D, Osabel D M. Equivalent SDOF Models for Estimating Isolation-Layer Energy
702 Dissipation in Base-Isolated Tall Buildings under Strong Winds[J]. Buildings, 2024, 14(2): 329.
703 [40] Hu X, Chen Q, Weng D, et al. Estimation of additional equivalent damping ratio of the damped
704 structure based on energy dissipation[J]. Advances in Civil Engineering, 2019, 2019(1): 8052413.
705 [41] Chen Y, Sato D, Miyamoto K, et al. Response-spectrum-based design method for active base-isolated
706 buildings with viscous dampers and hysteretic dampers[J]. Mechanical Systems and Signal Processing,

2022, 180: 109413.

[42] PEI Xingzhu，WANG Wei，WANG Xingxing．Earthquake response prediction of isolated structures based on energy principle［J］． Engineering Mechanics，2011，28 (7) : 66.

[43] GB/T 51408-2021; Standard for Seismic Isolation Design of Building. Ministry of Housing and Urban-Rural Development of China: Beijing, China, 2021.

[44] Kalpakidis I V, Constantinou M C, Whittaker A S. Modeling strength degradation in lead–rubber bearings under earthquake shaking[J]. Earthquake engineering & structural dynamics, 2010, 39(13): 1533-1549.

[45] Özdemir G. Formulations of equivalent linearization of lead-rubber bearings for incorporating the effect of lead core heating[J]. Earthquake Spectra, 2015, 31(1): 317-337.

[46] Higashino S, Kitamura H. Energy-balance based seismic response prediction methods for seismic isolated buildings with rubber bearings and viscous dampers[J]. J. Struct. Constr. Eng., AIJ, 2005 (588): 79-86.

[47] Ying Zhou, Mohammed Samier Sebaq, Yi Xiao,Energy dissipation demand and distribution for multi-story buildings with fluid viscous dampers,Engineering Structures,Volume 253,2022,113813,ISSN 0141-0296,https://doi.org/10.1016/j.engstruct.2021.113813.

[48] Bao Shun W, Hao Xiang H. Analytical Calculation of Damping Ratio and Performance-Based Design for Damage-Controlled Energy-Dissipation Structures[J]. Journal of Vibration Engineering,2022,35(02):264-276.DOI:10.16385/j.cnki.issn.1004-4523.2022.02.002.

[49] Afshin Moslehi Tabar, Dario De Domenico,Nonlinear response spectrum analysis of structures equipped with nonlinear power law viscous dampers,Engineering Structures,Volume 219,2020,110857,ISSN 0141-0296,https://doi.org/10.1016/j.engstruct.2020.110857.

[50] Vasile O, Bugaru M. A new modeling approach for viscous dampers using an extended Kelvin–Voigt rheological model based on the identification of the constitutive law’s parameters[J]. Computation, 2022, 11(1): 3.

[51] Dario De Domenico, Giuseppe Ricciardi,Improved stochastic linearization technique for structures with nonlinear viscous dampers,Soil Dynamics and Earthquake Engineering,Volume 113,2018,Pages 415-419,ISSN 0267-7261,https://doi.org/10.1016/j.soildyn.2018.06.015.

[52] Tubaldi E, Barbato M, Dall’Asta A. Performance-based seismic risk assessment for buildings equipped with linear and nonlinear viscous dampers[J]. Engineering Structures, 2014, 78: 90-99.

[53] Zhao Z, Wu M, Li Y, et al. Energy dissipation enhancement of nonlinear viscous damping-integrated negative stiffness amplifying dampers[J]. Nonlinear Dynamics, 2025, 113(8): 7731-7758.

[54] Han M, Liu X H, Du H K, et al. Experimental research on shearing properties of small lead-core rubber bearings[J]. J. Vib. Eng, 2024, 37(2): 326-335.

[55] Ahmadipour M, Alam M S. Sensitivity analysis on mechanical characteristics of lead-core steel-reinforced elastomeric bearings under cyclic loading[J]. Engineering Structures, 2017, 140: 39-50.

[56] Deringöl A H, Güneyisi E M, Hansu O. Combined effect of bearing stiffness of the base isolator and damping characteristics of the viscous damper on the nonlinear response of buildings[J]. International Journal of Steel Structures, 2022, 22(5): 1497-1517.

[57] Shen C Y, Huang X Y, Chen Y Y, et al. Factors affecting the dependency of shear strain of LRB and SHDR: experimental study[C]//Actuators. MDPI, 2021, 10(5): 98.

[58]KITAMURA H．Seismic response analysis methods for performance based design ［M］．Xi, an : Xi, an Jiaotong University Press，2004: 126.

[59] GB 50011-2010; Code for Seismic Design of Buildings. Ministry of Housing and Urban-Rural Development of China: Beijing, China, 2010.

[60] Tchamo J M, Xiao Y, Zhou Y. Mechanical Properties of Improved Multiple‐Layers Viscoelastic Damper[J]. Advances in Civil Engineering, 2023, 2023(1): 6374897.